Computed optical emissions from a sonoluminescing bubble

William C. Moss,* David A. Young, Judith A. Harte, Joanne L. Levatin, Balazs F. Rozsnyai, George B. Zimmerman, and I. Harold Zimmerman

Lawrence Livermore National Laboratory, P. O. Box 808, Livermore, California 94550

(Received 8 September 1998)

A sonoluminescing bubble has been modeled as a thermally conducting, partially ionized plasma. The model is more complete than previous models, due to the inclusion of both plasma and normal molecular thermal conduction, vapor pressure, surface tension, the mixing of gas and water vapor in the bubble, and opacities. The model accounts for most of the observed experimental trends, including (i) the asymmetric pulse shape; (ii) the temperature and driving pressure dependence of the pulse width and intensity; and (iii) spectral shapes, in particular, the 300-nm peak in the spectrum of xenon sonoluminescence, which to our knowledge has not been explained by any previous model; and (iv) a hydrodynamic explanation of why water is the ''friendliest'' liquid in which sonoluminescence occurs. The agreement between the calculations and the data, as well as the model's predictions of almost every experimental trend, suggest strongly that the spectral and temporal properties of the emissions of a sonoluminescing bubble are due to adiabatic- or shock-initiated thermal emission from a cool dense plasma. [S1063-651X(99)07503-0]

PACS number(s): 78.60.Mq, 43.25.+y, 52.35.Tc

I. INTRODUCTION

Single bubble sonoluminescence (SBSL) [1,2] is a phenomenon in which a liquid-filled flask contains an acoustically levitated gas-filled bubble that undergoes repeated cycles of growth and collapse in response to an applied acoustic standing wave. At the conclusion of each collapse, a brief flash of light is emitted by the gas bubble [3–5]. Although SBSL is relatively easy to achieve experimentally [6], the short duration of the flash ($\sim$100 ps), small radiating volume ($\sim 10^{-13}$ cm^3), and the extreme sensitivity of the data to experimental conditions make it difficult to acquire data sets that are complete enough to construct and validate theoretical models.

The complexity of SBSL data may prohibit a complete quantitative theoretical description. For example, bubble radii can be determined only to within a couple of microns [7,8]. While this represents a relatively small error with respect to $R_{\max}$ (the maximum bubble radius during the growth phase), the relative error in the accuracy of R_0 (the ambient bubble radius before the growth phase begins) can exceed 50%, which can have a large effect on the calculated emission. In addition, there are still no data sets that can be considered ''complete,'' from a theoretician's point of view: not only are R_0 and $R_{\max}$ required, but time dependent optical emission and spectra, for a range of driving pressures, liquid temperatures, and gas concentrations are also required. Therefore, from a practical point of view, we should expect no more from a theoretical model than the reproduction of experimental sensitivities to parameter variations, given the current experimental (and theoretical) uncertainties. Reproduction of the experimental trends indicates that the essential physics has been captured and builds confidence in the predictive capabilities of the model, even if precise quantitative agreement between theory and particular experimental data cannot be obtained.

*Electronic address: wmoss@llnl.gov

The current experimental features of SBSL that are appropriate for theoretical modeling are as follows: (i) The pulse width increases from $\sim$30 to $\sim$300 ps, as the amplitude of the driving pressure P_a near the bubble increases [4,5]. (ii) R_0 and $R_{\max}$ increase as P_a increases [7,8]. (iii) The maximum optical emission (with respect to P_a) increases as the temperature of the liquid surrounding the bubble decreases [9]. (iv) The air/argon SBSL spectral energy density has a peak $\leqslant$200 nm [10]. (v) The xenon SBSL spectral energy density has a broad peak at $\sim$300 nm [10].

Numerical solutions of the complete nonlinear hydrodynamic equations in the gas bubble and the surrounding liquid showed that many features of SBSL, including spectra, pulse widths, and the relative brightness of noble and diatomic gases, could be explained by thermal emission from a cool (few eV) dense plasma in the collapsed bubble [11]. The model included detailed high temperature and high density equations of state, plasma thermal conductivity ($\sim T^{5/2}$), and a temperature dependent greybody opacity, to calculate the optical emission. (The opacity determines the light intensity that is emitted at a given temperature.) The calculated results demonstrated the importance of the opacity, hydrodynamics, and the specific heat of the gas in the bubble, for determining the size of the radiating volume. The model showed that the bubble is like a tiny star; it emits from the surface of an optically thick core ($\sim$0.1 μm) that radiates through an optically thin radiating halo that surrounds the core. One of the main theoretical results of the cool dense plasma model is that a brighter bubble implies more radiating volume, not necessarily a higher temperature. Subsequent work, using the same model coupled with a chemical kinetics model of Lohse *et al.* [12], showed that the observed dependence of SBSL intensity on liquid temperature could also be explained [13].

Although the cool dense plasma model [11] provided physical insight into fundamental SBSL mechanisms, it was based on the limited experimental data that were available, so only the physics that was deemed relevant was included. Recent bubble dynamics data [7,8] and pulse width measure-

 ©1999 The American Physical Society

ments [4,5] justify the construction of a more complete model. In particular, we include (i) normal molecular thermal conductivity ($\sim T^{1/2}$) [14], to simulate the actual heat flow into and out of the bubble during expansion and collapse; (ii) temperature dependent surface tension, which affects the ambient gas pressure inside the bubble [14]; and (iii) ambient-condition dependent water vapor concentration [15], which affects $R_{\max}$ and the radiating volume [11]. In addition, we have also modified our plasma thermal conductivity model to provide a better representation of thermal conduction in the cool dense plasma in the collapsed bubble [16]. The only important physics missing from our model is viscosity, which has a negligible effect on the bubble dynamics [17], and evaporation/condensation and the associated mass transport in the bubble. We approximate the latter effect on the bubble dynamics using a water vapor pressure and a water vapor to gas ratio in the bubble whose time independent values vary with the initial ambient conditions.

In this paper, we show that the cool dense plasma model, with the approximations and refinements that are described above, gives an improved description of most of the observed features of SBSL, including (i) the asymmetric pulse shape; (ii) the temperature and driving pressure dependence of the pulse width and intensity; and (iii) spectral shapes, including the 300-nm peak in xenon SBSL; and (iv) a hydrodynamic explanation of why water is the ''friendliest'' liquid in which SBSL occurs.

II. MODEL

We assume spherical symmetry, and consider the motion of a bubble filled with a mixture of gas and water vapor, with an initial radius R_0 surrounded by a shell of water, whose outer radius is R_W. The gas, vapor, and liquid water are initially in thermal equilibrium, and at rest. The initial liquid pressure is P_0. The pressure in the bubble (gas plus water vapor) is balanced by the sum of the liquid pressure and the surface tension at the gas-liquid interface, so that the initial gas pressure is $P_0+2\sigma(T_0)/R_0-P_V(T_0)$, where σ and P_V are the surface tension and water vapor pressure. The outer radius of the water is driven by a sinusoidal pressure $P_0-P_A\sin 2\pi\nu t$. We calculate the bubble's response to a single cycle of the driving oscillatory pressure, that is, only one of the many growth and collapse cycles that the bubble experiences. We assume the physics that governs the creation of any one of the steady-state sonoluminescence flashes can be approximated using experimental values for $R_0, R_{\max}$, and ν, because the bubble collapse is primarily an inertial effect of the liquid compressing the gas.

Neglecting viscosity and mass diffusion, the equations for the conservation of mass and momentum for the system are [18,19]

$$\begin{aligned}
\frac{D\rho}{Dt} &= -\rho\nabla\cdot v,\\
\rho\frac{Dv}{Dt} &= -\nabla(P+Q),\\
P &= P_e(\rho,T_e)+P_i(\rho,T_i)+P_V(T_0)\big|_{\text{gas}},\\
P(R)\big|_{\text{gas}} &= P(R)\big|_{\text{liquid}}+2\sigma(T)/R,
\end{aligned} \tag{1}$$

where $D/Dt\equiv(\partial/\partial t)+v\cdot\nabla$, and ρ, v, $Q(|\nabla v|^2,\nabla v), P$, and σ are the density, velocity, artificial viscosity [20], pressure, and surface tension. The total pressure is the sum of the ion pressure, the electron pressure, and a constant vapor pressure P_v, which is included only in regions inside the bubble. The temperature dependent surface tension [21] creates a pressure jump across the gas-liquid interface. Conservation of energy is represented by separate equations for the ions and the electrons that include ion-electron coupling and thermal conduction. We write [18,19]

$$\begin{aligned}
\rho\frac{DE_i}{Dt} &= -(P_i+Q)\nabla\cdot v+\overline{K}_{ie}\\
&\quad\times(T_e-T_i)+\nabla\cdot(K_i\nabla T_i),\\
\rho\frac{DE_e}{Dt} &= -P_e\nabla\cdot v+\overline{K}_{ie}(T_i-T_e)+\nabla\cdot(K_e\nabla T_e),\\
E &= E_e(\rho,T_e)+E_i(\rho,T_i),\\
K_i &= K_0 c/c_0,\\
K_e &= 0.5kz^*n_i^{2/3}(1+z^{*1/3})^{-1}(3kT_e/m_e)^{1/2},
\end{aligned} \tag{2}$$

where $E_i, E_e, \overline{K}_{ie}, K_i$, and K_e are the ion and electron specific internal energies, the ion-electron coupling coefficient, and the ion and electron thermal conductivities, and $c, n_i k, m_e$, and z^* are the adiabatic sound speed, ion density, Boltzmann constant, electron mass, and degree of ionization [22]. A cool dense plasma ($\sim 1\,\text{g/cm}^3$ and ~ 2 eV) has a Debye length on the order of an angstrom [16,18], so that the range of Coulomb interactions is so short that the plasma behaves like a dense fluid whose transport properties are governed by collisions, rather than Coulomb interactions. Consequently, the conductivities in Eq. (2) can be constructed using simple kinetic theory [23], which yields $K=n_c k\lambda c_c/2$, where n_c is the number density of ''carriers,'' $\lambda=(n_{\text{sc}}\sigma)^{-1}$ is the mean free path between ''scatterers'' with number density n_{sc} and collision cross section σ, and c_c is the velocity of the ''carriers.'' Ion-ion collisions dominate the ion conductivity, because the ions are too massive to be scattered by the electrons, so $K_i\sim c\sim T^{1/2}$, which has the same form as normal molecular conductivity. The subscript ''o'' in Eq. (2) refers to ambient conditions. The electron thermal conductivity has contributions from electron-electron (ee) and electron-ion (ei) scattering. An effective mean free path is obtained by summing the collision rates: $v_e/\lambda_{\text{eff}}=v_e/\lambda_{\text{ee}}+v_e/\lambda_{\text{ei}}$, where $\lambda_{\text{ee}}=(z^*n_i)^{-1/3}$, $\lambda_{\text{ei}}=n_i^{-1/3}$, $v_e=(3kT_e/m_e)^{1/2}$, and the number density of electrons is z^*n_i. These collision rates can be used to calculate the electron-electron and ion-ion collision times, which in a cool dense plasma (~ 1 g/cm and ~ 2 eV) are 1 and 100 fs, respectively. The ions and electrons self-equilibrate and achieve well-defined temperatures within a few collisions. These equilibration times are at least two orders of magnitude less than experimental SL pulse widths. The thermal equilibration time between ions and electrons is no more than a few picoseconds, which is at least an order of magnitude less than the shortest SL pulse widths, so the ion and electron temperatures equilibrate rapidly everywhere except

TABLE I. Experimental data and calculational results. Simulations A1–C2 are based on the data of Gaitan and Holt [7] for sonoluminescing air bubbles. Simulations D1–D3 are based on the calculated bubble dynamics of Ref. [13]. Simulation E1 is based on representative data for sonoluminescing xenon bubbles [27]. Bold entries represent experimental data; ΔT_{expt} is from Ref. [5]; N_{expt} (bracketed values) are from Ref. [7], and represent their normalization of the relative number of emitted photons to C1. Unbracketed values of N_{expt} are from Ref.[9]. T_{th} is the maximum temperature at the surface of the optically thick region. T_{max} is the maximum temperature, which occurs at the center of the bubble. $P_0 = 1.013$ bar, except for B2. The driving frequency was 20.6 kHz for rows A, B, C, and E, and 26.5 kHz for row D. Additional data are given in Ref. [28]. P_a is the acoustic pressure near the bubble, and should not be confused with P_A, the driving pressure for the calculations.

ID	R_0 (μm)	R_{max} (μm)	T_0 (°C)	Water vapor (%)	ΔT (ps)	ΔT_{expt} (ps)	N (10^6)	N_{expt} (10^6)	$T_{\text{th}}/T_{\text{max}}$ (eV,eV)	Misc.	P_a (bar)
A1	**6.0**	**63.6**	**20**	40	85	~**160**	1.8	~**[10]**	1.6,11		**1.40**
A2	6.0	63.6	20	35	126		4.6		1.7,3.5		
A3	6.0	63.6	20	40	150		2.9		1.3,11	5κ	
A4	5.0	63.6	20	38	85		2.0		1.7,9.1		
B1	**4.0**	**48.8**	**20**	36	57	~**120**	0.74	~**[4]**	1.7,6.6		**1.32**
B2	4.0	56.1	20	36	66		1.2		1.8,7.5	$P_0 = .99$	
B3	4.0	39.8	20	36	42		0.21		1.5,5.1		
C1	**2.1**	**29.6**	**20**	30	32	~**90**	0.13	~**[1]**	1.8,4.1		**1.29**
C2	3.0	29.6	20	34	30		0.031		1.6,2.5		
D1	5.0	54.5	**2.5**	12	525		73	**6.0**	2.3,5.3		1.40
D2	4.0	39.8	**20**	36	46	~**120**	0.33	**0.5**	1.6,5.7		1.30
D3	3.5	32.9	**33**	76	2		1.8E-4	**0.01**	3.7,11		1.25
E1	**4.0**	**32.0**	**20**	36	290	~**200**	1.6		0.95,2.5		

near the center of the bubble, and T_i and $T_e$may be replaced by a single temperature field $T(r,t)$.

The equations of state for the gases, water, and water vapor were obtained from a combination of data and theory [24,25]. The equations of motion [Eqs. (1) and (2)] and the equations of state combined with the boundary and initial conditions given above can be solved numerically for the radial and temporal variation of all the field quantities.

Typical SBSL spectra can be integrated to show that the optical energy per flash is at most 10^{-6} of the thermal energy in the compressed bubble. Consequently, the photon field cannot affect the matter field. The short plasma collision times and the small amount of optically emitted energy relative to the thermal energy in the bubble create a condition of local thermodynamic equilibrium (LTE), which allows electron-photon coupling terms to be excluded from Eq. (2), thus simplifying the calculation of the emitted optical power [26]. The simplification introduced by LTE constrains the radiation source function to be the Planck function, and allows the emitted power to be computed entirely from the properties of the matter, specifically, ρ, T_e, and the opacity κ. The resulting expression for the emission from the surface of an optically thick core that radiates through an optically thin radiating halo that surrounds the core is [11]

$$(\text{Optical power}) = \int \eta(T_e)\sigma T_e^4 dA_{\text{th}} + \int_{R_{\text{th}}}^{R} 4\,\eta(T_e)\rho\kappa(\rho,T_e)\sigma T_e^4 dV, \quad (3)$$

where T_e varies spatially and temporally and σ, A_{th}, κ, R, and R_{th} are the fraction of the Planck spectrum between 200 and 750 nm, the surface area of the optically thick region, the Planck mean (frequency-averaged) opacity, the bubble radius, and the radius of the optically thick region. R_{th} is defined by the expression $1 = -\int_R^{R_{\text{th}}} \rho\kappa(\rho,T_e)dr$.

III. RESULTS

Table I shows the parameters for the calculations that were performed. The upper part of the table (rows A1–C2) shows simulations that are based on the experimental bubble dynamics data (R_0, R_{max}, and ν) of Gaitan and Holt (GH) [7] for air bubbles in water. We assume the validity of the rectification hypothesis [12,29], and perform our simulations using argon and water vapor filled bubbles, even though it has been shown that there are slight differences between air bubbles and argon bubbles [5]. A1, B1, and C1 represent three ''base'' calculations based on the GH data, whereas the other simulations represent sensitivity studies. Bold entries represent experimental data. Dashes represent unmeasured values. The lower part of the table (rows D1–D3) shows calculated bubble dynamics ''data'' (R_0, R_{max}, and ν) for water vapor and argon filled bubbles at three different ambient liquid temperatures [13]. The use of these calculated quantities for our sensitivity study was necessitated by the lack of experimental data. Representative bubble dynamics data for xenon (row E1) were obtained from Barber *et al.* [27].

Figure 1 shows the calculated expansion and initial col-

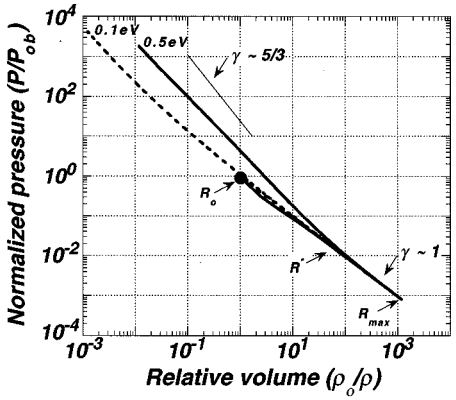

FIG. 1. Calculated expansion and initial collapse of a water vapor and argon filled bubble (data from Table I, row A1). The pressure is normalized by the ambient bubble pressure $P_{ob}=P_o+2\sigma(T_0)/R_0$. The small pressure difference between the initial expansion of the gas-liquid interface (dashed line) and the center of the bubble (solid line) is due to the finite time for heat to be conducted to the center of the bubble. The gas-liquid interface responds nearly isothermally ($\gamma\sim1$), whereas the center of the collapsing bubble begins to respond adiabatically at $R^*(R\sim4R_0)$. The peak temperatures and pressures that are shown in the figure occur 300 ps before the sonoluminescence flash.

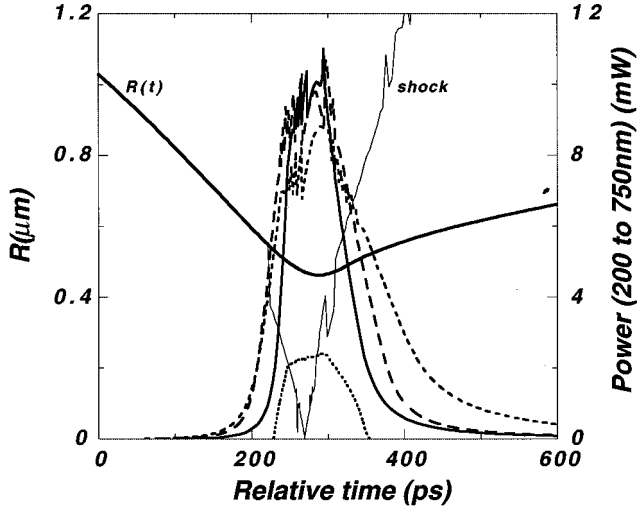

FIG. 2. The conclusion of the collapse shown in Fig. 1. The figure shows the time dependence of the bubble radius $R(t)$ (thick solid line), the collapse induced shock wave (thin solid line), and the optically thick region (dotted line). The other thick solid line shows the emitted optical power. The pulse width increases, as the water vapor content decreases from 40% to 35% (long dashed line; the calculated power has been multiplied by 0.5, and the abscissa has been displaced by -85 ps to compare the calculations). Increasing the opacity by a factor of 5 (short dashed lines) increases the pulse width further. See Table I for additional results.

lapse of a water vapor and argon filled bubble, using row A1 in Table I. The figure shows the pressure at the center of the bubble (solid line) and just inside the gas-liquid interface (dashed line), both normalized to the ambient pressure in the bubble. The dot shows the ambient conditions. The expansion and initial collapse occurs nearly isothermally throughout the bubble: $\gamma=d(\ln P)/d(\ln\rho)\sim1$, where γ is the polytropic exponent [30]. Although the periphery of the bubble collapses isothermally until $R\sim R_0$, the center of the bubble begins to make a transition from isothermal to adiabatic behavior early in the collapse. This behavior is typical of all the calculated results in Table I. The figure shows that the often-used approximation of describing the gas in the bubble using a single spatially independent pressure (and temperature) can introduce errors, even if a compressional-dependent γ is used.

The specific heat ratio at the center of the bubble never reaches 5/3, because of the presence of water vapor, whose detailed treatment we discuss next. As the bubble expands, the gas pressure decreases and the bubble fills with water vapor. The expansion is slow with respect to typical thermal diffusion times, so the bubble fills isothermally with water vapor at a constant pressure $P_v(T_0)$, which also represents approximately the minimum pressure in the bubble during expansion. We cannot currently model evaporation and condensation and the changing mass in the bubble, but we can account for the dynamics, by never allowing the pressure in the bubble to be less than $P_v(T_0)$. This accounts properly for the PdV work done by the vapor during the expansion, and increases the calculated value of $R_{\max}$by a few microns. As the bubble begins to collapse, water vapor condenses and is removed from the interior of the bubble. As the collapse accelerates, condensation cannot occur rapidly enough, so vapor becomes trapped inside the bubble, which affects the hydrodynamics of the collapse. In particular, the concentration of trapped water vapor affects the size of the radiating region. As the percentage of trapped water vapor increases, the γ of the mixture decreases and the bubble heats more inhomogeneously, which produces a very large and rapid temperature increase near the center of the bubble. Although the center of the bubble can be very hot, the total radiating volume decreases due to the inhomogeneous heating, so there is actually less optical emission [11]. The detailed mixing is beyond the scope of our current model, but we can approximate its average effect on the hydrodynamics of the collapse by assuming a fixed molar ratio of water vapor and gas that scales with the initial ambient conditions [31]. The values shown in Table I were referenced to the arbitrarily chosen 40% value that was used for the simulation shown in Fig. 1.

Figure 2 shows the conclusion of the collapse shown in Fig. 1. The thick solid line shows the time dependence of the bubble radius $R(t)$. The thin solid line shows the trajectory of a shock wave that is generated near the conclusion of the collapse, which reflects from the center of the bubble at $t=270$ ps. (Numerical noise is responsible for the jaggedness of the curves.) The other solid line shows the power emitted [Eq. (3)] between 200 and 750 nm. 1.8 M photons are emitted in a 85 ps full width at half maximum (FWHM) pulse that is due to both adiabatic and shock heating, because emission begins before there is significant shocking. Although the compression creates an optically thick region (dotted line in the figure) near the center of the bubble, most of the emission is from the optically thin halo that surrounds the optically thick region. The surface temperature of the optically thick region never exceeds 1.6 eV (19 000 K).

The asymmetry of $R(t)$ around $R_{\min}$ gives rise to the asymmetry of the computed pulse shape, which shows a shorter rise time than fall time, and a ''tail,'' in agreement

with experimental data [4,32]. The emitted power (solid line) is unchanged when there is no thermal conduction during the 600 ps that are shown in Fig. 2, which indicates that the thermal diffusion time is long and that adiabatic expansion is the dominant cooling mechanism. This conclusion modifies the results of earlier calculations [11], which neglected normal thermal conduction during the growth and initial collapse.

The dashed lines show the sensitivity of the emitted power ''base'' calculation (solid line) to changes in only the water vapor content or the opacity. 4.6 M photons are emitted in a 126 ps FWHM pulse when the vapor content is reduced from 40% to 35% (long dashed line), whereas 2.9 M photons are emitted in a 150 ps FWHM pulse (short dashed line) when the opacity is multiplied by a factor of 5. (The calculated opacities are only accurate to within a factor of 10 for these cool dense plasmas.) We could claim that any of these results agree with the experimental data [5].

Figure 2 shows that the emitted photons and pulse width decrease significantly, as the water vapor concentration increases (Table I, rows A1 and A2). As shown in Fig. 1, water vapor lowers the effective γ of the bubble contents. The sound speed decreases as γ decreases, so it is easier to generate a shock in the bubble. Consequently, the bubble heats more inhomogeneously, with a higher maximum temperature at the center of the bubble (compare $T_{\max}$ for A1 and A2), but with a decrease in the total volume that is hot enough to emit appreciably. This explains why sonoluminescence from noble gas bubbles ($\gamma \sim \frac{5}{3}$) is brighter than from diatomic gases ($\gamma \sim \frac{7}{5}$) [11]. A lower γ means that more compressional energy goes into internal degrees of freedom than into heating the bubble, even though stronger shock waves are produced. The stronger the shock wave, the shorter the pulse width, which explains why air SBSL has a shorter pulse width than argon SBSL [5]. Although the Lohse hypothesis [12] is generally true, clearly some air remains in the bubble from cycle to cycle. The air, which has a lower γ than argon, further enhances the inhomogeneous heating, shocking, and shortening of the pulse width. The preceding analysis also provides a hydrodynamic explanation of why water is the ''friendliest'' liquid for SBSL: the vapor of most other polyatomic liquids will have a γ even lower than water, so that even more energy is lost to internal degrees of freedom, producing an even smaller radiating volume, with perhaps too few photons to measure. The concomitant enhancement of the shock that results from a smaller γ may also decrease the stability of the bubble. It would seem that from a *purely hydrodynamic perspective* liquid argon would be an ideal substitute for water in SBSL experiments.

Figure 3 shows the experimental (solid lines) [10] and calculated (dashed lines) wavelength dependence of the spectral energy density of argon and xenon bubbles undergoing SL. Reference [10] did not include bubble dynamics data, so we used the GH $R_0 = 2.1$ and 6.0 μm bubble dynamics data (A1 and C1) from Table I to calculate bounding values for the argon spectrum and the xenon $R_0 = 4.0$ μm bubble dynamics data (E1) to calculate a representative spectrum for xenon. The calculations reproduce the general features of the data, despite the experimental and theoretical uncertainties. The peak in the xenon spectrum, which to our knowledge has not been explained previously by any other

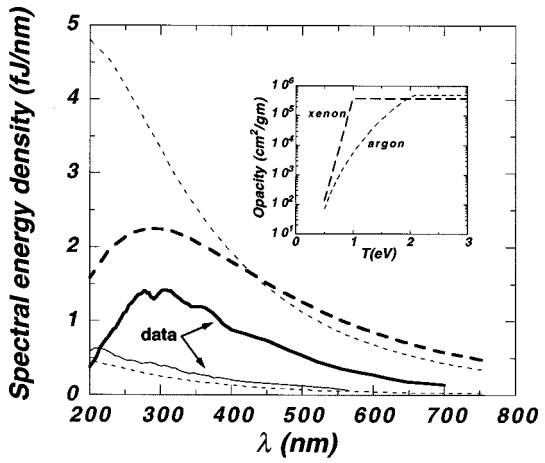

FIG. 3. Wavelength (λ) dependence of experimental (solid lines) and calculated (dashed lines) SBSL spectra for xenon (thick lines) and argon (thin lines). The calculations reproduce the general features of the experimental data, including the 300 nm peak for xenon. The inset shows the calculated opacities for argon and xenon.

hydrodynamic model, is a simple consequence of the temperature dependence of the opacity. This peak has also been observed in theoretical spectra resulting from electron–neutral-atom bremsstrahlung [33]. Consider the spatial profile of temperature in the bubble at an instant of time during the collapse. The temperature increases as the center of the bubble is approached. The inset in Fig. 3 shows that the opacity of xenon increases more rapidly than that of argon, as the temperature increases [34]. Consequently xenon becomes optically thick at a larger radius and lower temperature than argon. The emission is characterized approximately by a temperature no greater than that at the surface of the optically thick region, since it is not possible to ''see'' into the bubble any further than one optical thickness. The measured peak in the xenon spectral energy density at 300 nm corresponds to an emitting temperature of $\sim$0.9 eV, which is consistent with our calculation. The absence of a peak in the argon data indicates an emitting temperature greater than 1.2 eV, which is also consistent with our calculations. the temperature dependence of the opacity is also responsible for xenon SBSL having a longer pulse width than argon, because xenon begins (and ceases) to emit at a lower temperature than argon; that is, xenon emission begins earlier in the collapse and continues longer during the re-expansion of the bubble than for argon. Figures 2 and 3 reiterate the importance of the opacity for describing the spectral and temporal characteristics of SBSL emission.

Table I shows that the model can account for the main experimental trends of the data. For example, the number of emitted photons and the pulse width increase as the driving acoustic pressure P_a increases (rows C1, B1, and A1). The bracketed entries in the table represent measured quantities that were normalized by Gaitan and Holt to experiment C1. Our equivalent normalized number of emitted photons agrees with the GH data given the experimental and theoretical uncertainties. We note that if only pure argon bubbles are considered (0% water vapor), then the emission ratio between calculations A1 and C1 exceeds 100, which is much greater

than the experimental value. The water vapor influences strongly the size of the radiating volume, and is necessary for the agreement between the calculated and experimental emission ratios.

It is well known experimentally that the maximum optical emission from SBSL increases as the liquid temperature decreases. Previous calculations [13] confirmed this observation, as do our current calculations (rows D1–D3). The discrepancies at 2.5 and 33 °C are due to the percentage of water vapor, which is obtained from our approximation [31] of the full water vapor dynamics, to which our calculations are quite sensitive (compare A1 and A2). Nevertheless, the calculated variation with temperature is consistent with the data. Calculations B1 and B3 show that a small change in only R_{max} can produce nearly a factor of four difference in the number of emitted photons. Calculations A3 and A4, and C1 and C2 show that changes in R_0 that are well within experimental error can produce large changes in the pulse width and number of emitted photons. These calculations show generally that the pulse width and number of emitted photons increase as R_{max}/R_0 increases, but there can be exceptions due to the extreme nonlinearity of the physics.

We consider changes in the ambient pressure P_0 [35], as a final example of the extreme sensitivity of the calculated results to initial or experimental conditions. Calculations B1 and B2 are identical except for a difference of 0.023 bar in ambient pressure, which is representative of the difference in barometric pressure between a rainy and a sunny day, or ~200 m of elevation. The calculated pulse width increases by 15% and the number of emitted photons nearly doubles when the ambient pressure is lowered (rainy day, or higher elevation), which again emphasizes the difficulties of comparing and modeling experimental data in detail.

IV. CONCLUSIONS

Although a theoretical model can be used to understand the fundamental mechanisms of a particular phenomenon, it can also be used predictively. A model's utility and eventual acceptance as the probable description of a particular phenomenon is based on its ability to describe existing data and experimental trends, and to predict experimental results and perhaps novel consequences before the experiments are performed. We have shown that our model of SL as thermal emission from a cool dense plasma can explain the major features and trends of the data that are available currently. We now make the following predictions, based on our model: (i) the maximum SBSL intensity should increase as water vapor content decreases (increasing γ); (ii) SBSL should be brighter on a cloudy day, or at higher elevations (decreasing P_0); (iii) there should be more red than blue photons in the tail of an SBSL pulse; (iv) for low water vapor content (near freezing), the xenon or argon optical pulse may have two peaks that are separated by tens of picoseconds (the bubble begins to radiate at smaller compressions, due to the large γ, as R decreases; the pulse width is long and thermal conduction is slow, so two peaks appear because the radiating volume decreases, then increases as R passes through R_{min}); (v) replacing liquid water with liquid argon, and using a helium bubble should produce very bright SBSL, based on hydrodynamic considerations; and (vi) spectral lines may be visible from a weakly driven helium bubble (bound-bound transitions in helium).

It has been nine years since the discovery of SBSL. Although many theoretical models have been proposed, our model's predictions of almost every experimental trend suggest strongly that the spectral and temporal properties of SBSL are due to adiabatic- or shock-initiated thermal emission from a cool dense plasma.

ACKNOWLEDGMENTS

We thank D. Boercker and F. Rogers for interesting discussions about dense plasmas. Technical critiques by T. Gay and T. Matula, and funding from N. Burkhard, are appreciated greatly. This work was performed under the auspices of the U. S. Department of Energy by Lawrence Livermore National Laboratory under Contract No. W-7405-Eng-48.

[1] D. F. Gaitan, Ph.D. thesis, University of Mississippi, 1990 (unpublished).
[2] D. F. Gaitan, L. A. Crum, C. C. Church, and R. A. Roy, J. Acoust. Soc. Am. **91**, 3166 (1992).
[3] B. P. Barber and S. J. Putterman, Nature (London) **352**, 318 (1991).
[4] B. Gompf, R. Günther, G. Nick, R. Pecha, and W. Eisenmenger, Phys. Rev. Lett. **79**, 1405 (1997).
[5] R. A. Hiller, S. J. Putterman, and K. R. Weninger, Phys. Rev. Lett. **80**, 1090 (1998).
[6] R. A. Hiller and B. P. Barber, Sci. Am. (Int. Ed.) **272** (2), 96 (1995).
[7] D. F. Gaitan and R. G. Holt, Phys Rev. E (to be published).
[8] T. J. Matula (unpublished).
[9] B. P. Barber, C. C. Wu, R. Löfstedt, P. H. Roberts, and S. J. Putterman, Phys. Rev. Lett. **72**, 1380 (1994).
[10] R. Hiller, K. Weninger, S. J. Putterman, and B. P. Barber, Science **266**, 248 (1994).
[11] W. C. Moss, D. B. Clarke, and D. A. Young, Science **276**, 1398 (1997).
[12] D. Lohse, M. P. Brenner, T. F. Dupont, S. Hilgenfeldt, and B. Johnston, Phys. Rev. Lett. **78**, 1359 (1997).
[13] S. Hilgenfeldt, D. Lohse, and W. C. Moss, Phys. Rev. Lett. **80**, 1332 (1998).
[14] V. Q. Vuong and A. J. Szeri, Phys. Fluids **8**, 2354 (1996).
[15] K. Yasui, Phys. Rev. E **56**, 6750 (1997).
[16] F. MacIntyre (unpublished).
[17] S. Hilgenfeldt, M. P. Brenner, S. Grossman, and D. Lohse, J. Fluid Mech. **365**, 171 (1998).
[18] Ya. B. Zel'dovich and Yu. P. Raizer, *Physics of Shock Waves and High-Temperature Hydrodynamic Phenomena* (Academic, New York, 1966), Chaps. I–III, and VII.
[19] G. B. Zimmerman and W. L. Kruer, Thermonuclear Fusion **2**, 51 (1975); contains a description of the LASNEX hydrocode.
[20] J. von Neumann and R. D. Richtmyer, J. Appl. Phys. **21**, 232

(1950); artificial viscosity is used for the numerical stability of shock waves and is not a real material viscosity.

[21] $\sigma(T)=\mathrm{Max}[0,\sigma_{\mathrm{ref}}(T-T_c)/(T_{\mathrm{ref}}-T_c)]$; *Handbook of Chemistry and Physics*, 76th ed., edited by D. R. Lide (CRC Press, Boca Raton, FL, 1995), pp. 6–10 and 11; $T_c=374$ °C. $\sigma_{\mathrm{ref}}=0.0727$ N/m, and $T_{\mathrm{ref}}=20$ °C.

[22] z^* is obtained from the equation of state or from LASNEX [19].

[23] F. Reif, *Fundamentals of Statistical and Thermal Physics* (McGraw-Hill, New York, 1965), Chap. 12.

[24] D. A. Young (unpublished).

[25] D. A. Young and E. M. Corey, J. Appl. Phys. **78**, 3748 (1995).

[26] G. C. Pomraning, *The Equations of Radiation Hydrodynamics* (Pergamon, New York, 1973), pp. 44–49.

[27] B. P. Barber, R. A. Hiller, R. Löfstedt, S. J. Putterman, and K. R. Weninger, Phys. Rep. **28**, 65 (1997).

[28] *Handbook of Chemistry and Physics* (Ref. [21]), pp. 6–10, P_v (2.5, 20, and 33 °C)=0.0074, 0.023, and 0.05 bar; p. 6-251, $K_0^{\mathrm{xenon}}(20\ ^\circ\mathrm{C})=5.37$ mW/mK; p. 6-24, K_0^{argon} (2.5, 20, and 33 °C)=16.6, 17.2, and 18.2 mW/mK; p. 6-10, K_0^{water}(2.5, 20, and 33 °C)=566, 598, and 620 mW/mK.

[29] T. J. Matula and L. A. Crum, Phys. Rev. Lett. **80**, 865 (1998).

[30] T. G. Leighton, *The Acoustic Bubble* (Academic, San Diego, 1994), pp. 10 and 11.

[31] The molar fraction of water vapor is computed by scaling the calculated fraction for the $R_0=6$ μm and $T_0=20$ °C ambient condition and normalizing arbitrarily to 40%. The percent of water vapor is equal to

$$21.62\,\frac{P_V(T_0)}{P_0+2\sigma(T_0)/R_0}.$$

[32] R. Pecha, B. Gompf, G. Nick, Z. Q. Wang, and W. Eisenmenger, Phys. Rev. Lett. **81**, 717 (1998).

[33] L. Frommhold, Phys. Rev. E **58**, 1899 (1998).

[34] B. Rozsnyai, Defense Res. Rev. **1**, 21 (1981).

[35] L. Kondic, C. Yuan, and C. Chan, Phys. Rev. E **57**, 32 (1998).